This article has been accepted for publication in a future issue of this journal, but has not been fully edited. Content may change prior to final publication. Citation information: DOI 10.1109/TIE.2020.3009568, IEEE Transactions on Industrial Electronics

Fast Eye-in-Hand 3D Scanner-Robot Calibration for Low Stitching Errors

Xingjian Liu, Harikrishnan Madhusudanan, Wenyuan Chen, Dahai Li, Ji Ge, Changhai Ru, and Yu Sun

***Abstract*—This paper proposes a new eye-in-hand 3D scanner-robot calibration approach to realize low data stitching errors during long-term continuous measurement. Eye-in-hand 3D scanner-robot systems are commonly used for complete measurement of an object under test (OUT) from multiple fields of view (FOVs). To align the multiple FOVs into a single coordinate system, marker-free stitching assisted by robot's positioning is attractive since it bypasses the cumbersome traditional fiducial marker-based method. Based on periodically capturing calibration images from a 2D calibration target, scanner's and robot kinematic model's parameters are optimized. The challenges overcome in this work include, (1) how to compensate for the center-detection error in scanner calibration; (2) how to avoid the dependency of hand-eye calibration on DH parameters; and (3) how to calculate an accurate world-to-robot transformation. These challenges were tackled by several new techniques including accurate scanner calibration with iterative refinement of control points, virtual arm-based scanner-robot kinematic modeling, and trajectory-based world-to-robot transformation calculation. Experimental results demonstrated a low initial stitching error similar to the fiducial marker-based method (0.0446 mm vs. 0.0542 mm) was achieved. The mean stitching error was effectively maintained to be $<$0.1 mm during the continuous measurement with an average intermittent downtime of 78 seconds for recalibration.**

***Index Terms*—Robot sensing systems, manufacturing automation, industrial metrology, structured light measurement, kinematic model, data stitching.**

The authors acknowledge financial support from the Natural Sciences and Engineering Research Council of Canada, the Canada Research Chairs program, and the Ontario Research Fund - Research Excellence program. They also acknowledge technical support by Mr. Cheng Zeng and Dr. Yu Lin from Kirchhoff Automobile North America Inc. *(X. Liu and H. Madhusudanan contributed equally to this work.) (Corresponding author: Yu Sun.)*

X. Liu, H. Madhusudanan, Dahai Li, and J. Ge are with the Department of Mechanical and Industrial Engineering, University of Toronto, Toronto, ON M5S 3G8, Canada, and also with the Robotics Institute, University of Toronto, Toronto, ON M5S 3G8, Canada. (e-mail: xj.liu@utoronto.ca; harikrishnan.madhusudanan@mail.utoronto.ca; dahai.li@utoronto.ca; geji1981@gmail.com).

W. Chen is with the Department of Electrical and Computer Engineering, University of Toronto, Toronto, ON M5S 3G8, Canada, and also with the Robotics Institute, University of Toronto, Toronto, ON M5S 3G8, Canada. (e-mail: chenwy.chen@mail.utoronto.ca).

C. Ru is with the Research Center of Robotics and Micro System, Soochow University, Suzhou 215021, China, and also with the Jiangsu Provincial Key Laboratory of Advanced Robotics, Soochow University, Suzhou 215021, China. (e-mail: rzh@suda.edu.cn).

Y. Sun is with the Department of Mechanical and Industrial Engineering, University of Toronto, Toronto, ON M5S 3G8, Canada, and also with the Robotics Institute, the Department of Electrical and Computer Engineering, and the Department of Computer Science, University of Toronto, Toronto, ON M5S 3G8, Canada. (e-mail: sun@mie.utoronto.ca).

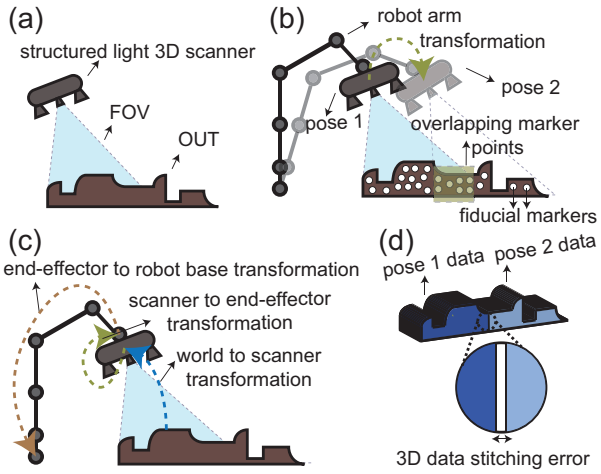

Fig. 1. (a) Structured light 3D scanning of an object. The relative transformation between multiple poses is obtained by using fiducial markers (b) or robot kinematics (DH parameters) and hand-eye transformation (c). (d) Data captured at multiple poses are stitched together.

I. Introduction

OPTICAL measurement of three-dimensional (3D) surface geometry has gained wide applications in industrial inspection [1], visual servoing [2], and vision-guided automation [3]. Among these 3D optical measurement methods, structured light-based scanning has the advantages of high-accuracy, non-contact, and full-field characteristics [4]. In most applications, the object under test (OUT) is larger than a single field-of-view (FOV) of the 3D scanner (see Fig. 1(a)). For complete measurement, the 3D scanner is usually mounted on a robotic arm (eye-in-hand) to acquire point clouds from multiple FOVs of the object (see Fig. 1(b)(c)). To achieve high quality of 3D point clouds, a data stitching process is required to align the multiple FOVs into a single coordinate system.

Fiducial marker-based [5], [6] and robot kinematics-based methods [7], [8] are the two mainstream approaches for data stitching. In fiducial marker-based method (Fig. 1(b)), placing markers on every industrial part and removing them is cumbersome. Furthermore, not all object surfaces are suitable or allowed for attaching markers. In contrast, the robot kinematics-based method does not require marker placement. It transfers point clouds of multiple FOVs from the scanner's coordinate frame to a common robot base frame to achieve data stitching. The accuracy of the merged point clouds depends on accurate calibration of scanner's parameters (world to scanner), hand-eye parameters (scanner to end-effector), and robot's Denavit-Hartenberg (DH) parameters [9] (end-effector to robot base)

0278-0046 (c) 2020 IEEE. Personal use is permitted, but republication/redistribution requires IEEE permission. See http://www.ieee.org/publications_standards/publications/rights/index.html for more information.
Authorized licensed use limited to: The University of Toronto. Downloaded on August 22,2020 at 19:39:02 UTC from IEEE Xplore. Restrictions apply.

This article has been accepted for publication in a future issue of this journal, but has not been fully edited. Content may change prior to final publication. Citation information: DOI 10.1109/TIE.2020.3009568, IEEE Transactions on Industrial Electronics

(Fig. 1(c)). However, the aforementioned parameters deteriorate over time due to factors such as wear, gear backlash and temperature changes [10], [11], leading to high 3D data stitching errors (>0.2 mm) [12]. Long-term routine industrial operation demands automated, accurate, and fast calibration of scanner, hand-eye, and DH parameters to maintain low data stitching errors.

Scanner calibration is necessary for extracting 3D geometric information from captured 2D images (world to scanner). Among existing methods, 2D target-based calibration methods [13]–[16] gained widespread adoption because of its high flexibility. It gives a closed-form solution from a set of matches between known target points and their 2D image points, where squares [13], chessboard [14] and circles [15], [16] are commonly used 2D features. Since square/chessboard detection is more sensitive to illumination conditions, circle-based targets are often used for high-accuracy calibration [15], [16]. Existing circle-based techniques directly detect the circle centers on the captured images as the calibration algorithm's inputs; however, these images suffer from inherent optics-caused nonlinear distortions [17], causing detection errors in scanner calibration.

For hand-eye (scanner to end-effector) calibration and the calibration of robot's DH parameters (end-effector to robot base), there exist several techniques. Hand-eye calibration is performed by solving an equation of the form $\mathbf{AX} = \mathbf{XB}$ [18], [19]. $\mathbf{X}$ is the unknown hand-eye transformation to determine. $\mathbf{A}$ is the relative transformation of scanner frame between different poses. $\mathbf{B}$ is the relative transformation of end-effector frame between different poses, which is a function of DH parameters. However, the accuracy of DH parameters deteriorates over time as discussed above, causing inaccuracies in hand-eye calibration and further high 3D data stitching errors. Although there are methods for calibrating DH parameters separately using optical [20], [21] and laser tracking systems [22], [23] by tracking a specialized target attached to the robot's end-effector, the long downtime (e.g., 10-15 minutes for mounting and removing specialized target [21], [22]) poses limitations for their application in long-term routine industrial use. To prevent the inaccuracies in hand-eye calibration due to errors in DH parameters, the dependency of hand-eye transformation on DH parameters should be avoided such that they can be calibrated and optimized simultaneously.

For long-term operation, kinematic parameters should be optimized regularly to reduce errors overtime. To construct the cost function for optimization, accurate transformation $\mathbf{Z}$ from the calibration target (world) to the robot base frame needs to be known as the ground truth reference [24]. Although methods exist for robot-world calibration by solving the equation of the form $\mathbf{AX} = \mathbf{ZB}$ [25], [26], where $\mathbf{Z}$ is the unknown world-to-robot transformation, errors present in the DH parameters are not considered. These errors bias the calculation of $\mathbf{Z}$ and the subsequent optimization of the scanner-robot kinematic model. Thus, automated, accurate, and fast calibration of scanner-robot parameters remains unsolved.

A new calibration technique to reduce large 3D data stitching errors and long calibration-caused system downtime is proposed in this paper. For periodic recalibration in order to maintain a low data stitching error, the robot moves towards a 2D standard calibration target and optimizes the entire system parameters with significantly reduced downtime, after which 3D scanning resumes. The problems tackled in this work include: (1) how to compensate for the center-detection error in scanner calibration; (2) how to avoid the dependency of hand-eye calibration on DH parameters such that robot and hand-eye parameters can be calibrated at the same time; (3) how to calculate the accurate world-to-robot transformation $\mathbf{Z}$ (for constructing cost function in optimization) without involving imperfect DH parameters.

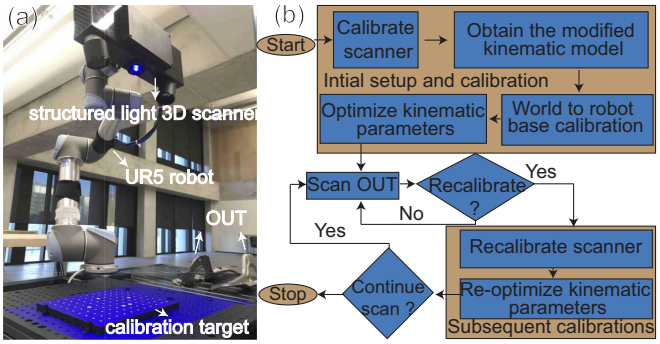

Fig. 2. (a) System setup: a structured light scanner mounted on a robot arm. (b) Overall operation sequence of the initial system setup, initial calibration, OUT scan and subsequent recalibration when needed.

The proposed calibration technique solves these challenges by integrating several novel key techniques including accurate scanner calibration with iterative refinement of circle centers (Section III), scanner-robot kinematic model modification via a virtual-arm technique (Section IV), and trajectory-based world-to-robot transformation calculation (Section V). Experimental results demonstrate that the 3D scanner-robot system is capable of achieving a low initial stitching error similar to the fiducial marker-based method (0.0446 mm vs. 0.0542 mm) was achieved. The mean stitching error was effectively maintained to be <0.1 mm during the continuous measurement with an average downtime of 78 seconds for recalibration.

II. System Overview

A. System Setup

The system used in this work (Fig. 2(a)) consists of a custom-built standard 3D structured light scanner and a 6-axis robot arm (UR5). The scanner consists of standard components, including two cameras (Basler acA2440-20gm, resolution: 2448×2048 pixels) and a projector (Texas Instruments ANSI lumens RGB LED). The cameras and projector are synchronized by an external triggering circuit at a frame rate of 20 Hz. With the selected hardware, the 3D scanner has an FOV of 300 mm×400 mm at the working distance of 700 mm. A standard certified 2D calibration target with an array of circles was used. An automotive part larger than the FOV of the scanner was used as OUT.

0278-0046 (c) 2020 IEEE. Personal use is permitted, but republication/redistribution requires IEEE permission. See http://www.ieee.org/publications_standards/publications/rights/index.html for more information.
Authorized licensed use limited to: The University of Toronto. Downloaded on August 22,2020 at 19:39:02 UTC from IEEE Xplore. Restrictions apply.

This article has been accepted for publication in a future issue of this journal, but has not been fully edited. Content may change prior to final publication. Citation information: DOI 10.1109/TIE.2020.3009568, IEEE Transactions on Industrial Electronics

B. Operation Sequence

As shown in Fig. 2(b), during the initial setup, the scanner parameters are calibrated first. Next, the kinematic model of the scanner-robot system is modified to remove the dependency of hand-eye transformation on DH parameters. The calibration target-to-robot base frame transformation $\mathbf{Z}$ (world-to-robot) is obtained as the ground-truth for optimizing system kinematic parameters. With the modified kinematic model and the ground truth world-to-robot transformation, a cost function is defined. The subsequent optimization step minimizes this cost function using the 2D calibration target. Since the initial calibration parameter errors can be large, initial optimization takes longer than subsequent optimizations. After the optimization step, the robot turns towards the OUT and the scanner performs scanning on the OUT. In subsequent recalibrations, the resultant parameters obtained from the previous optimization step are used as estimated values to speed up the optimization process. Calibration of scanner and the kinematic parameters are repeated when required to maintain a low data stitching error.

III. Scanner Calibration

Scanner calibration involves calibrating the scanner's intrinsic (Λ_l, Λ_r for intrinsic matrices, d_l, d_r for distortion coefficients) and extrinsic parameters (Γ_s for translation from left to right camera and Γ_l from world to left camera) [15], [16]. In this work, a 2D calibration target is used with N feature points printed on it. The scanner is moved in M different positions and orientations with the 2D calibration target in its FOV. Via center detection [27], 2D centers $x_l^{mn} \in \mathbb{R}^2$ and $x_r^{mn} \in \mathbb{R}^2$ are detected on the left and right image planes, where m denotes the m^{th} pose of the calibration target and n denotes the n^{th} feature point on the target. Since the design of the calibration target is known, the 3D world coordinates of n^{th} feature point can be obtained and denoted as $X_w^n \in \mathbb{R}^3$. With these as input, the unknowns are firstly calculated by a closed-form solution [13], and then a globally optimal estimation (bundle adjustment [15]) is used to adjust the parameters to minimize the following cost function.

$$\xi = \{\hat{\xi}_l, \hat{\xi}_r, \hat{X}_w^{1:N}\} = \underset{\xi_l, \xi_r, X_w^{1:N}}{\arg\min} \left(cst(\xi_l, \xi_r, X_w^{1:N})\right) \quad (1)$$

where $\xi_l = (\Lambda_l, d_l, \Gamma_l^{1:M})$ and $\xi_r = (\Lambda_r, d_r, \Gamma_r^{1:M})$ are left and right camera parameters and the cost function cst is

$$\begin{cases} cst(\xi) = \sum_{m=1}^{M} \sum_{n=1}^{N} (\frac{1}{2}\chi_l^{mn} + \frac{1}{2}\chi_r^{mn}) \\ \chi_l^{mn} = \|x_l^{mn} - \hat{x}_l^{mn}\|^2 \\ \chi_r^{mn} = \|x_r^{mn} - \hat{x}_r^{mn}\|^2 \\ \hat{x}_l^{mn} = \Psi_l(\Lambda_l, d_l, \Gamma_l^m, X_w^n) \\ \hat{x}_r^{mn} = \Psi_r(\Lambda_r, d_r, \Gamma_s, \Gamma_r^m, X_w^n) \end{cases} \quad (2)$$

in (2), $\hat{x}_l^{mn} \in \mathbb{R}^2$ and $\hat{x}_r^{mn} \in \mathbb{R}^2$ are called predicted image points which are a group of 2D image projections of $X_w^n \in \mathbb{R}^3$ with existing system parameters (by closed-form solution or previous optimization). $\Psi_l/\Psi_r : \mathbb{R}^3 \rightarrow \mathbb{R}^2$ represent the function projecting 3D world coordinates to the 2D image plane with system parameters. By combining (1) and (2), the optimal estimation boils down to minimizing the reprojection errors (χ_l^{mn} and χ_r^{mn}) between the control points (x_l^{mn}, x_r^{mn}) and predicted image points ($\hat{x}_l^{mn}, \hat{x}_r^{mn}$). The reprojection error quantifies how closely an estimate of system parameters recreates the point's true projection [28].

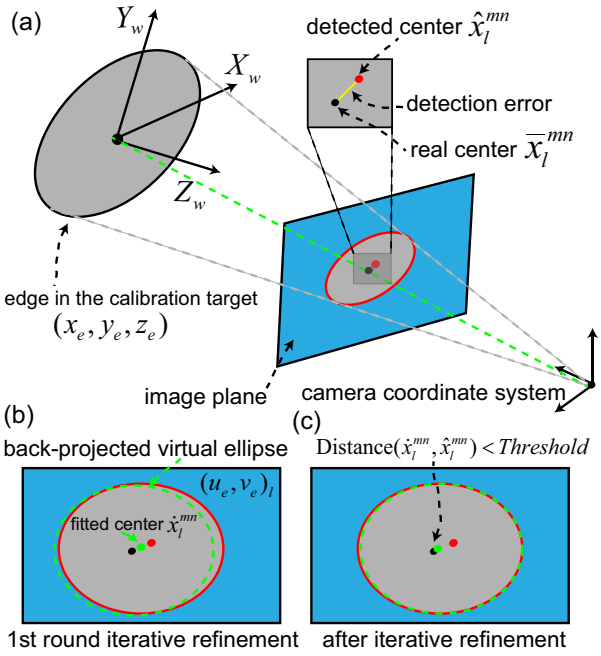

Fig. 3. (a) Perspective projection and lens distortion cause detection error of a circular control point. The real center of circular control point is not coincident with the detected center position in the image plane, resulting in poor calibration accuracy. (b) Fitted center $\dot{x}_l^{mn}$ from projected virtual ellipse $(u_e, v_e)_l$ falls in between original detected center x_l^{mn} (red) and real center (black) in the first iteration. (c) Fitted center $\dot{x}_l^{mn}$ approaches real center after iterative refinements.

A limitation of the traditional calibration method [15], [16] is that the detected control points x_l^{mn} and x_r^{mn} are regarded as ground truth and kept fixed during optimization. However, for a circular control point, it often becomes a distorted ellipse in the image plane because of perspective projection and lens distortion [17], causing the real center to deviate from the detected center, as illustrated in Fig. 3(a). The detection error of x_l^{mn} and x_r^{mn} can lead to inaccurate scanner calibration. The error in scanner calibration also propagates to subsequent hand-eye and robot kinematics model calibration, resulting in poor accuracy in 3D data stitching.

To overcome this limitation, we propose an iterative refinement approach to compensate for the detection error. Instead of using the detected control points from distorted 2D images, the 3D circles (edge points) on the calibration target are projected and undistorted to the image plane by the initial calibrated system parameters. The obtained 2D contours of these 3D circles are used to fit the 2D centers of control points with higher accuracy because they are undistorted by the initial calibration parameters. Once the control points are localized, they are then used to recompute the camera calibration parameters. This process is repeated until convergence.

In the first iteration, traditional calibration algorithm is

0278-0046 (c) 2020 IEEE. Personal use is permitted, but republication/redistribution requires IEEE permission. See http://www.ieee.org/publications_standards/publications/rights/index.html for more information.
Authorized licensed use limited to: The University of Toronto. Downloaded on August 22,2020 at 19:39:02 UTC from IEEE Xplore. Restrictions apply.

This article has been accepted for publication in a future issue of this journal, but has not been fully edited. Content may change prior to final publication. Citation information: DOI 10.1109/TIE.2020.3009568, IEEE Transactions on Industrial Electronics

conducted to calculate the initial estimate of system parameters ξ_{init}. In the subsequent iterations, the edge points of 3D circles ($X_e(x_e, y_e, z_e)$) are calculated first. With the known 3D world coordinates of centers $X_w^n = (x_c, y_c, z_c)$ and circle's radius r_c, the edge point X_e is

$$\begin{cases} (x_e - x_c)^2 + (y_e - y_c)^2 + (z_e - z_c)^2 = r_c^2 \\ a(x_e - x_c) + b(y_e - y_c) + c(z_e - z_c) = 0 \end{cases} \tag{3}$$

With obtained $X_e = (x_e, y_e, z_e)$ in 3D world coordinates and initial system parameters ξ_{init}, these edge points are projected and undistorted to the left and right image plane, respectively. A group of virtual ellipses are then obtained in the image plane, $(u_e, v_e)_l = \Psi_l(\Lambda_l, d_l, \Gamma_l^m, X_e)$ and $(u_e, v_e)_r = \Psi_r(\Lambda_r, d_r, \Gamma_s, \Gamma_r^m, X_e)$, as shown in Fig. 3(b). These virtual ellipses are used to fit the updated control points $\dot{x}_l^{mn}$ and $\dot{x}_r^{mn}$,

$$\begin{cases} \dot{x}_l^{mn} = EllipseFitting(u_e, v_e)_l \\ \dot{x}_r^{mn} = EllipseFitting(u_e, v_e)_r \end{cases} \tag{4}$$

Substituting these updated control points into (2) gives

$$\begin{cases} cst(\xi) = \sum_{m=1}^{M} \sum_{n=1}^{N} (\frac{1}{2}\chi_l^{mn} + \frac{1}{2}\chi_r^{mn}) \\ \chi_l^{mn} = \|\dot{x}_l^{mn} - \Psi_l(\Lambda_l, d_l, \Gamma_l^m, X_w^n)\|^2 \\ \chi_r^{mn} = \|\dot{x}_l^{mn} - \Psi_r(\Lambda_r, d_r, \Gamma_s, \Gamma_r^m, X_w^n)\|^2 \end{cases} \tag{5}$$

This process is iterated according to (3)-(5) until the distance between updated control points $\dot{x}_l^{mn}$ and $\dot{x}_l^{mn}$ and previous control points x_l^{mn} and x_l^{mn} is smaller than a predefined threshold (e.g., 0.1 pixel) (see Fig. 3(c)).

IV. Virtual Arm-based Kinematic Model

After accurate scanner calibration, the transformation from the scanner frame to robot base frame must be determined so that point clouds from multiple FOVs can be transferred into a single coordinate frame. Traditionally, robot parameters are calibrated using optical/laser tracking systems [20]–[22] and the hand-eye transformation $\mathbf{X}$ is calibrated separately by solving an equation of the form $\mathbf{AX} = \mathbf{XB}$ [18], [19], where $\mathbf{X}$ is the unknown hand-eye transformation; $\mathbf{A}$ is the relative transformation of scanner frame between different poses; and $\mathbf{B}$ is the relative transformation of end-effector between different poses which is a function of DH parameters. Using this hand-eye transformation $\mathbf{X}$ and the DH parameters, the scanner frame's position and orientation with respect to the robot base frame can be represented as

$$\begin{cases} {}_{i-1}^{i}\mathbf{DH} = Tran_{z_{i-1}}(d_i) Rot_{z_{i-1}}(\theta_i) Tran_{x_i}(a_i) Rot_{x_i}(\alpha_i) \\ \mathbf{X} = \begin{bmatrix} R_X & T_X \\ 0^T & 1 \end{bmatrix} \\ \mathbf{T}_{\mathbf{scanner}}^{\mathbf{robot}} = {}_{0}^{1}\mathbf{DH}\ {}_{1}^{2}\mathbf{DH} \dots {}_{4}^{5}\mathbf{DH}\ {}_{5}^{6}\mathbf{DH}\,\mathbf{X} \end{cases} \tag{6}$$

where ${}_{i-1}^{i}\mathbf{DH}, i = 1, \dots, 6$ denotes the homogeneous transformation from joint i frame to joint $i-1$ frame (see Fig. 4(a)). The DH parameters $(a_i, d_i, \alpha_i, \theta_i)$ represent the link length, link offset, link twist and joint angle of the i^{th} link, respectively. However, the DH parameters undergo changes overtime due to non-geometric factors such as wear and temperature changes, causing inaccuracies in $\mathbf{X}$. This requires periodic calibration of robot DH parameters by using optical/laser tracking systems, followed by hand-eye calibration since the accuracy of $\mathbf{X}$ is dependent on DH parameters [20], [22], [23]. The long downtime (10-15 minutes [22]) of this procedure is undesired for long-term routine industrial operation.

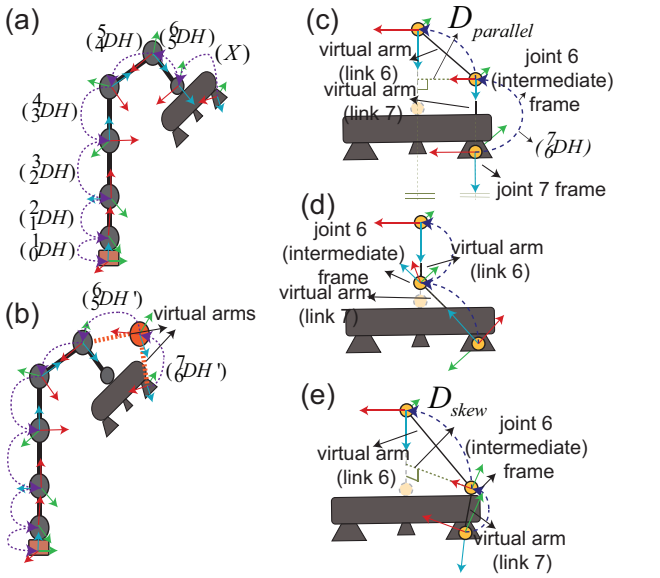

Fig. 4. (a) Determination of the transformation from scanner to robot base frame using hand-eye transformation and DH parameters. (b) Construction of intermediate frame and virtual arm links. (c) Construction of intermediate frame when $\mathbf{z}$-axis) of scanner frame is parallel to that of joint 5 frame. (d) Construction of intermediate frame when $\mathbf{z}$-axis) of scanner frame intersects with that of joint 5 frame. (e) Construction of intermediate frame when $\mathbf{z}$-axis) of scanner frame is skew with that of joint 5 frame.

To avoid the dependency of hand-eye transformation on DH parameters, our technique modifies the existing kinematic model such that both robot and hand-eye parameters can be calibrated at the same time. This is accomplished by constructing a new set of DH parameters for transformation from scanner frame to joint 5 frame of the robot. However, the new parameters cannot be constructed directly because using DH representation, only translation and rotation about two axes ($\mathbf{x}$ and $\mathbf{z}$) can be represented [9].

To overcome this limitation, an intermediate joint frame is inserted in between scanner frame and joint 5 frame with two new virtual arm links, as shown in Fig. 4(b). Hence, the transformation from the scanner frame to robot base frame can be represented using purely DH parameters as

$$\begin{cases} \mathbf{T}_{\mathbf{scanner}}^{\mathbf{robot}} = [{}_{0}^{1}\mathbf{DH} \dots {}_{4}^{5}\mathbf{DH}][{}_{5}^{6}\mathbf{DH}'\ {}_{6}^{7}\mathbf{DH}'] \\ {}_{i-1}^{i}\mathbf{DH} = Tran_{z_{i-1}}(d_i) Rot_{z_{i-1}}(\theta_i) Tran_{x_i}(a_i) Rot_{x_i}(\alpha_i) \\ {}_{k-1}^{k}\mathbf{DH}' = Tran_{z_{k-1}}(d_i') Rot_{z_{k-1}}(\theta_k') Tran_{x_k}(a_k') Rot_{x_k}(\alpha_k') \end{cases} \tag{7}$$

where ${}_{i-1}^{i}\mathbf{DH}, i = 1, \dots, 5$ is the same in (6), and ${}_{k-1}^{k}\mathbf{DH}', k = 6, 7$ are are the transformations from the scanner frame to the intermediate frame and from the intermediate frame to joint 5 frame, respectively. $(a_k', d_k', \alpha_k', \theta_k')$ are the newly constructed DH parameters of the 6^{th} and 7^{th} links.

0278-0046 (c) 2020 IEEE. Personal use is permitted, but republication/redistribution requires IEEE permission. See http://www.ieee.org/publications_standards/publications/rights/index.html for more information.
Authorized licensed use limited to: The University of Toronto. Downloaded on August 22,2020 at 19:39:02 UTC from IEEE Xplore. Restrictions apply.

This article has been accepted for publication in a future issue of this journal, but has not been fully edited. Content may change prior to final publication. Citation information: DOI 10.1109/TIE.2020.3009568, IEEE Transactions on Industrial Electronics

The location of the intermediate frame depends on the orientation of scanner frame with respect to joint 5 frame. The initial position and orientation of the scanner frame with respect to joint 5 frame (${}^{6}_{5}\mathbf{DH}\,\mathbf{X}$) is determined with the traditional hand-eye calibration approach. Although this transformation may not be accurate at this moment due to the presence of initial errors in DH parameters, the inaccuracies are eliminated in the next step through optimization (Section V). Based on the type of scanner and robot used, the **z**-axis of the scanner frame and joint 5 frame can either be parallel, intersecting, or skew (neither parallel nor intersecting), respectively. In the following steps to construct DH parameters, joint 5 frame is considered as the frame of reference.

1) **Parallel (Fig. 4(c))**. The center point of the intermediate frame (P_0) is selected anywhere along the **z**-axis of the scanner frame. Let P_1 be any point along the **z**-axis of the joint 5 frame. From P_0, the **x**-axis of the intermediate frame is constructed along the shortest distance line to the **z**-axis of joint 5 frame. The distance of this line is
$$D_{parallel} = \frac{|P_0 \times (P_0 - P_1)|}{|P_1|} \tag{8}$$
The **z**-axis of the intermediate frame is along the direction of **z**-axis of the scanner frame.
2) **Intersecting (Fig. 4(d))**. The center point of the intermediate frame is chosen to be at the point of intersection, and **x**-axis is perpendicular to the plane formed by the two intersecting **z**-axis. The **z**-axis of the intermediate frame is along the **z**-axis of the scanner frame.
3) **Skew (Fig. 4(e))**. The center point is chosen at a point on the **z**-axis of the scanner frame where a line perpendicular to the **z**-axis of both joint 5 frame and scanner frame meets, and **x**-axis is along this shortest distance line. The distance of this line is
$$D_{skew} = \frac{|P_3 \cdot (P_2 \times (P_4 - P_3))|}{|P_2 \times (P_4 - P_3)|} \tag{9}$$
In (9), P_2 is any point on the **z**-axis of joint 5 frame; P_3, P_4 are any two points on the **z**-axis of the scanner frame.

The **x**-axis of the intermediate frame is along this calculated shortest distance line. D_{skew} (or $D_{parallel}$ in the case of parallel **z**-axis) represents the link length (a'_6) DH parameter of the intermediate joint frame. Note that, in the case of intersecting **z**-axis, $a'_6 = 0$. Based on the position and orientation of the intermediate frame with respect to joint 5 frame and the scanner frame with respect to the intermediate frame, the remaining DH parameters for the intermediate frame and the scanner frame are constructed according to traditional methods [9] with the original DH parameters replaced for joint 6, and joint 7 added to the kinematic chain. The process of obtaining the modified kinematic model involves capturing few poses, which costs 5-7 seconds, and is performed only once during initial system setup.

V. Trajectory-based World-to-Robot Transformation Calculation

The modified kinematic parameters are optimized for error reduction. To perform optimization, an accurate calibration target to robot base (world-to-robot) transformation $\mathbf{Z}^{\mathbf{robot}}_{\mathbf{world}}$ is calculated to construct the cost function. Existing methods [25], [26], which find this world-to-robot transformation by solving an equation of the form $\mathbf{AX} = \mathbf{ZB}$, cannot be used in this case because errors in DH parameters are propagated to the world-to-robot transformation $\mathbf{Z}^{\mathbf{robot}}_{\mathbf{world}}$. In contrast, our proposed technique is based only on the trajectory points formed by the scanner frame with respect to the calibration target (world) frame, without any DH parameters involved.

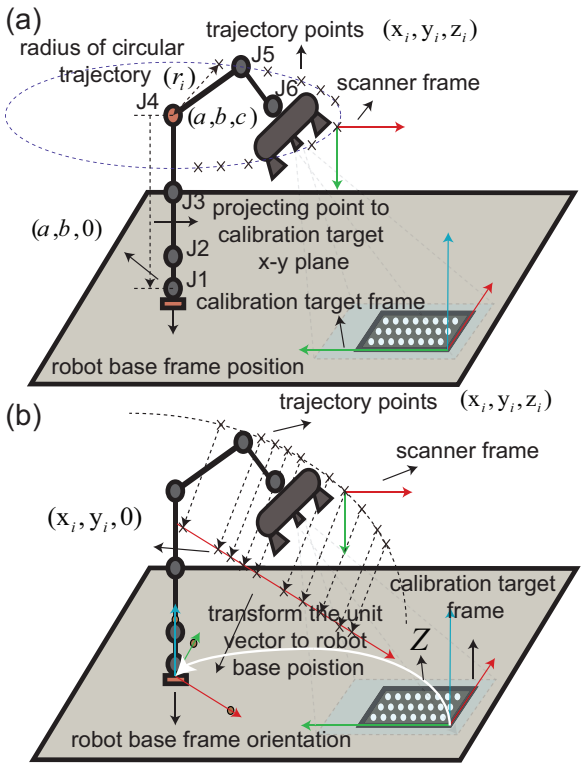

Fig. 5. (a) Determining the position of robot base frame with respect to calibration target frame using circular trajectory. (b) Determining the orientation of robot base frame with respect to calibration target frame using linear trajectory.

To find the robot base frame position with respect to the calibration target frame, only the base joint (J1) of the robot (see in Fig. 5(a)) is moved for any $n(>3)$ different angles to keep all other joint angles (J2-J6) fixed such that the calibration target is always entirely within the FOV of the scanner. Since the kinematic model of the system has been modified as discussed in Section IV, the original point of scanner frame is regarded as the virtual end-effector. For these n different poses of the robot, n trajectory points of the virtual end-effector are recorded by calculating the transformation from calibration target frame to scanner frame using the PnP algorithm [29]. This forms a circular trajectory of n points in 3D space. A common center $P_c(a,b,c)$ satisfying all these points is

$$\begin{cases} P_c = \underset{(a,b,c)}{\arg\min} \sum_{i=0}^{n-1} \sum_{j=i}^{n} (\gamma(x_i,y_i,z_i)^2 - \gamma(x_j,y_j,z_j)^2) \\ \gamma(x,y,z) = \sqrt{(a-x)^2 + (b-y)^2 + (c-z)^2} \end{cases} \tag{10}$$

0278-0046 (c) 2020 IEEE. Personal use is permitted, but republication/redistribution requires IEEE permission. See http://www.ieee.org/publications_standards/publications/rights/index.html for more information.
Authorized licensed use limited to: The University of Toronto. Downloaded on August 22,2020 at 19:39:02 UTC from IEEE Xplore. Restrictions apply.

This article has been accepted for publication in a future issue of this journal, but has not been fully edited. Content may change prior to final publication. Citation information: DOI 10.1109/TIE.2020.3009568, IEEE Transactions on Industrial Electronics

where (x_i, y_i, z_i) are the coordinates of the i^{th} trajectory point, $\gamma(x_i, y_i, z_i)$ is the radius of circular trajectory of the i^{th} point. The sum of difference between the squared radius of two adjacent trajectory points ($\gamma(x_i, y_i, z_i)$ and $\gamma(x_j, y_j, z_j)$) is minimized to find the center of the best fit circle $P_c(a, b, c)$. Once the best fit circle P_c is obtained, it is projected to the $\mathbf{x}$-$\mathbf{y}$ plane of the calibration target frame by setting c to 0. Hence, $(a, b, 0)$ is the required robot base frame position with respect to the calibration target frame. The $\mathbf{z}$-axis of robot base frame is parallel with that of calibration target frame.

The $\mathbf{z}$-axis of the UR5 robot base frame is perpendicular to the base plane of the robot, and when base joint angle (J1) is at 0 degree, J2 rotates along the $\mathbf{y}$-axis of the robot base frame. Thus, to determine the $\mathbf{x}$-axis of robot base frame as shown in Fig. 5(b), J1 angle is fixed at 0 degree and only J2 is rotated for n different angles. All other joint angles are fixed such that the calibration target frame is entirely within the scanner's FOV. For each point, the position of the virtual end-effector is determined with respect to the calibration target frame by the PnP algorithm [29].

These points are projected down to the $\mathbf{x}$-$\mathbf{y}$ plane of calibration target frame by setting their $\mathbf{z}$ component to zero. Fitting a best line to these trajectory points is conducted to determine the $\mathbf{y}$-axis direction of the robot base frame. (x_{mid}, y_{mid}) is defined as the mean center point on the best fit line containing all the points. (x_i, y_i) is the coordinates of the i^{th} trajectory point. The best fit line is

$$\begin{cases} y = kx + m \\ k = \dfrac{\sum_{i=1}^{n}((x_i - x_{mid})(y_i - y_{mid}))}{\sum_{i=1}^{n}(x_i - x_{mid})^2} \\ m = y_{mid} - kx_{mid} \end{cases} \tag{11}$$

The unit vector along the direction of this line $y = kx + m$ towards the calibration target is determined and translated to the robot base frame position. In this way, the $\mathbf{x}$-axis of robot base frame is determined (see Fig. 5(b)). Together with the known $\mathbf{z}$-axis, $\mathbf{y}$-axis is found using the right-hand rule. Based on this position and orientation, the homogenous transformation $\mathbf{Z}^{\mathbf{robot}}_{\mathbf{world}}$ from the robot base to the calibration target frame is obtained. In this technique, the errors from the DH parameters are avoided by moving only one joint at a time. The only other source of error in tracking the trajectory points can be from incorrect scanner calibration. Thus, the scanner parameters are accurately calibrated using the scanner calibration technique as described in Section III. However, irrespective of scanner calibration the obtained $\mathbf{Z}^{\mathbf{robot}}_{\mathbf{world}}$ transformation remains the same as the errors in the circular and linear trajectory are compensated by fitting a best circle and line, respectively.

Using the modified kinematic model and the obtained world-robot transformation $\mathbf{Z}^{\mathbf{robot}}_{\mathbf{world}}$ as the ground truth, a cost function is constructed, and the model parameters are optimized using iterative nonlinear optimization. n different views of the calibration target are captured with different robot poses. For the i^{th} pose of the robot, let ${}^{i}\mathbf{H}^{\mathbf{world}}_{\mathbf{scanner}}$ be the transformation obtained from the calibration target frame to the scanner frame using the PnP method, ${}^{i}\mathbf{T}^{\mathbf{scanner}}_{\mathbf{robot}}(a_{1-7}, d_{1-7}, \alpha_{1-7}, \theta_{1-7})$ be the transformation from the scanner frame to the robot base frame which is a function of modified kinematic parameters to be optimized including link length a_{1-7}, link offset d_{1-7}, link twist α_{1-7} and joint angle θ_{1-7}. For the i^{th} pose, the estimated transformation ${}^{i}\mathbf{C}^{\mathbf{world}}_{\mathbf{robot}}$ from the calibration target (world) to robot base is

$${}^{i}\mathbf{C}^{\mathbf{world}}_{\mathbf{robot}}(a_{1-7}, d_{1-7}, \alpha_{1-7}, \theta_{1-7}) = {}^{i}\,\mathbf{T}^{\mathbf{scanner}}_{\mathbf{robot}}\ {}^{i}\mathbf{H}^{\mathbf{world}}_{\mathbf{scanner}}. \tag{12}$$

Let $\mathbf{R}_{\mathbf{i_C}}$ and $\mathbf{t}_{\mathbf{i_C}}$ be the rotational and translation components of ${}^{\mathbf{i}}\mathbf{C}^{\mathbf{robot}}_{\mathbf{world}}$. $\mathbf{R}_{\mathbf{Z}}$, and $\mathbf{t}_{\mathbf{Z}}$ be the rotational and translational components of $\mathbf{Z}^{\mathbf{robot}}_{\mathbf{world}}$. For n different poses, the position error (PE$(a_{1-7}, d_{1-7}, \alpha_{1-7}, \theta_{1-7})$) and orientation error (OE$(a_{1-7}, d_{1-7}, \alpha_{1-7}, \theta_{1-7})$) are

$$\begin{cases} PE = \sum_{i=1}^{n} ||[\mathbf{t}_{\mathbf{z}} - \mathbf{t}_{\mathbf{i_C}}]\,[\mathbf{t}_{\mathbf{z}} - \mathbf{t}_{\mathbf{i_C}}]'|| \\ OE = \sum_{i=1}^{n} ||[Rodrigues(\mathbf{R}_{\mathbf{i_C}}\,\mathbf{R}'_{\mathbf{z}})]\,[Rodrigues(\mathbf{R}_{\mathbf{i_C}}\,\mathbf{R}'_{\mathbf{z}})]'|| \end{cases} \tag{13}$$

where $r_v = Rodrigues(R)$ is the Rodrigues' rotation formula which transfers rotation matrix $R \in \mathbb{R}^{3\times3}$ to a rotation vector $r_v \in \mathbb{R}^{1\times3}$. Then the objective function is

$$E = \underset{a_{1-7}, d_{1-7}, \alpha_{1-7}, \theta_{1-7}}{\arg\min} (PE + OE) \tag{14}$$

Minimization is performed with respect to $(\partial a_{1-7}, \partial d_{1-7}, \partial \alpha_{1-7}, \partial \theta_{1-7})$, which corresponds to deviations of link length, link offset, link twist and joint angle of links 1 to 7 (the virtual arm-based kinematic model in Section IV), respectively. Optimization is subject to $|\partial a_{1-7}| \le e_a, |\partial d_{1-7}| \le e_d, |\partial \alpha_{1-7}| \le e_\alpha, |\partial \theta_{1-7}| \le e_\theta$, where $(e_a, e_d, e_\alpha, e_\theta)$ are the constraints, and their values are set based on maximum expected deviation in the modified kinematic parameters. This is a non-linear optimization model with bounded constraints, which is commonly solved by sequential quadratic programming [30], [31].

VI. Experimental Results and Discussion

A. Performance of Scanner Calibration

To evaluate the performance of our scanner calibration technique, a standard certified 2D calibration target was used. The target consists of 99 circles with a diameter of 5 ± 0.001mm for the small circles and 10 ± 0.001 mm for the large circles. The distance between two adjacent circles is 20 ± 0.001 mm. The mean measurement error of the distance between the adjacent circles, ε_c, was used as the metric for scanner calibration evaluation.

$$\varepsilon_c = \frac{\sum_{i=1:N} |\sqrt{(p_i - p_{i+1})^2} - 20.0|}{N} \tag{15}$$

where p_i is 3D coordinate of the reconstructed circle centers with calibrated parameters.

The proposed iterative refinement with center detection error compensation for scanner calibration was compared with the traditional scanner calibration approach [15]. Since temperature change is a main factor causing scanner measurement

0278-0046 (c) 2020 IEEE. Personal use is permitted, but republication/redistribution requires IEEE permission. See http://www.ieee.org/publications_standards/publications/rights/index.html for more information.
Authorized licensed use limited to: The University of Toronto. Downloaded on August 22,2020 at 19:39:02 UTC from IEEE Xplore. Restrictions apply.

This article has been accepted for publication in a future issue of this journal, but has not been fully edited. Content may change prior to final publication. Citation information: DOI 10.1109/TIE.2020.3009568, IEEE Transactions on Industrial Electronics

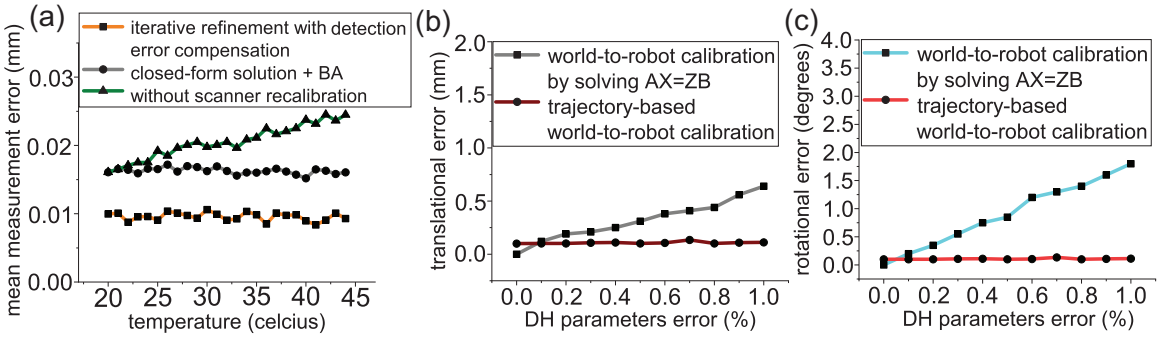

Fig. 6. (a) Scanner calibration. Mean measurement error by our proposed method based on iterative refinement of circular feature points, the traditional closed-form approach with bundle adjustment, and without scanner recalibration. Comparison of translational error (b) and rotational error (c) between traditional world-to-robot calibration and our proposed trajectory-based world-to-robot calibration.

errors [32], we manually increased the surrounding temperature of the scanner from 20°C to 45°C with a heater. For each measurement, 20 different images were captured from different poses and both the proposed and traditional calibration were conducted to obtain the scanner parameters and reconstruct 3D coordinates of the calibration target. The experimental results are shown in Fig. 6 (a). It can be seen that, without regular calibration (i.e., only with initial calibration using the traditional method), the mean measurement error was 0.015 mm. As the scanner temperature was gradually increased from 20°C to 45°C, the mean measurement error increased from 0.015 mm to 0.025 mm. When recalibration was performed regularly using the traditional method, a consistent mean measurement error of 0.016 mm was maintained. In comparison, calibration using our proposed technique outperformed the traditional method, which achieved a mean measurement error of 0.01 mm throughout the process due to its capability of compensating for circle detection errors.

B. Performance of $\mathbf{Z}^{\mathbf{robot}}_{\mathbf{world}}$ Transformation Calculation

The world-to-robot transformation $\mathbf{Z}^{\mathbf{robot}}_{\mathbf{world}}$ obtained by our proposed method was compared with that by the traditional method by solving $\mathbf{A_n X} = \mathbf{Z}^{\mathbf{robot}}_{\mathbf{world}}\mathbf{B_n}$. $\mathbf{A_n}$ is the set of relative transformations between scanner frame obtained from n different poses $[\mathbf{A_1}, \ldots, \mathbf{A_n}]$. $[\mathbf{B_1}, \ldots, \mathbf{B_n}]$ is the set of relative transformations between end-effector frames obtained from n different poses as a function of DH parameters. $\mathbf{X}$ is the scanner-to-end effector transformation. The main drawback of the traditional method is that the errors present in DH parameters bias the calculation of $\mathbf{Z}^{\mathbf{robot}}_{\mathbf{world}}$.

For each measurement of world-to-robot transformation $\mathbf{Z}^{\mathbf{robot}}_{\mathbf{world}}$, n = 10 different poses were taken. Artificial errors were added (up to 1% with an interval of 0.1%) to all the 24 DH parameters (six links) of the robot. The transformation obtained using the traditional method initially when no error was added to the DH parameters was considered to be the nominal value $\mathbf{Z}^{\mathbf{robot}}_{\mathbf{world(nominal)}}$. The rotational and translational error metrics, defined in [33], are

$$\begin{cases} Err(R_Z^{measured}) = \left\| R_Z^{nominal} - R_Z^{measured} \right\| \\ Err(t_Z^{measured}) = \left\| t_Z^{nominal} - t_Z^{measured} \right\| \end{cases} \quad (16)$$

where $R_Z^{measured}$ and $t_Z^{measured}$ are the rotational and translational components of world-to-robot transformation obtained using our proposed method and the traditional method ($\mathbf{AX} = \mathbf{ZB}$). The rotational and translational errors between the nominal world-to-robot transformation and calculated world-to-robot transformation for both methods were compared, as summarized in Fig. 6(b)(c). As the errors in DH parameters increased, the rotational and translational errors of world-to-robot transformation increased gradually for the traditional method. In contrast, our proposed trajectory-based world-to-robot calculation method achieved consistently low errors irrespective of increase in errors of DH parameters. The results demonstrate that our proposed method is independent of errors in DH parameters.

C. Evaluation of Virtual Arm-Based Kinematic Model

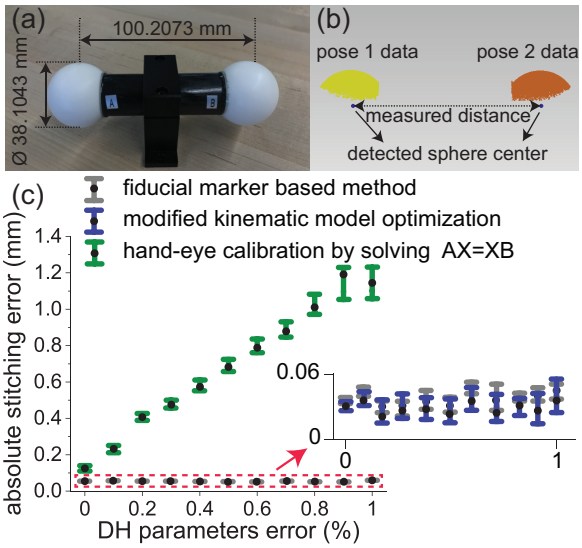

Fig. 7. (a) Standard ball-bar used for quantifying 3D data stitching error. (b) Stitched 3D point cloud captured from two different poses. (c) Absolute data stitching error by modified kinematic model optimization, fiducial marker-based method, and traditional hand-eye calibration. Each measurement was repeated ten times.

Since DH parameters deteriorate over time in long-term operation and errors in DH parameters cause inaccuracies

0278-0046 (c) 2020 IEEE. Personal use is permitted, but republication/redistribution requires IEEE permission. See http://www.ieee.org/publications_standards/publications/rights/index.html for more information.
Authorized licensed use limited to: The University of Toronto. Downloaded on August 22,2020 at 19:39:02 UTC from IEEE Xplore. Restrictions apply.

This article has been accepted for publication in a future issue of this journal, but has not been fully edited. Content may change prior to final publication. Citation information: DOI 10.1109/TIE.2020.3009568, IEEE Transactions on Industrial Electronics

in hand-eye calibration and subsequent 3D data stitching, we modified the standard kinematic model with a virtual arm-based model. A certified standard ball-bar was measured (Fig. 7 (a)) to evaluate the performance of the virtual arm-based kinematic model. The ball-bar has a center-to-center distance of 100.2073 mm as verified by a coordinate measuring machine (CMM). The ball-bar was scanned from two different poses to capture one ball at a time in each pose, and the data were stitched together, as shown in Fig. 7 (b). The metric of absolute measurement error is

$$\varepsilon_d = |L_m - L_b| \tag{17}$$

where L_m is the measured distance and L_b represents the CMM-measured data.

In the experiment, the scanner was calibrated using the proposed calibration technique first. Then errors up to 1% with an interval of 0.1% were artificially added to all the 28 DH parameters (seven links) of the robot to mimic the elongation of the robot links due to increase in temperature over time. To prove the repeatability of the result, each measurement was performed ten times with different relative position and orientation of the ball-bar with respect to the robot base frame for each added error percentage, and the average absolute stitching error was quantified. Performance of the virtual arm-based kinematic model was compared with that of the fiducial marker-based method, and that of the traditional hand-eye calibration by solving the equation of the form $\mathbf{AX} = \mathbf{XB}$ with erroneous DH parameters.

As seen in Fig. 7 (c), with the traditional hand-eye calibration (i.e., using erroneous DH parameters and hand-eye transformation), a data stitching error of 1.1638 mm was obtained for 1% of DH error. This is because of bias in the $\mathbf{X}$ calculation in solving $\mathbf{AX} = \mathbf{XB}$ due to errors in DH parameters. Differently, our modified kinematic model integrates scanner frame into the original kinematic model by using the virtual-arm technique, and the modified model is represented by pure DH parameters which can be calibrated and optimized in one go. For each DH error percentage, our proposed method and fiducial marker-based method achieved similar mean stitching errors without significant differences (0.0446 mm vs. 0.0542 mm, p = 0.525). These results prove that our proposed method is immune to errors in DH parameters and is capable of achieving similar data stitching accuracies as the cumbersome fiducial marker-based method.

D. Overall Performance Evaluation

In this experiment, a part of a large automotive car cross beam (CCB) (600 mm x 300 mm) was measured firstly by a Faro CMM (ScanArm) to generate benchmarking data. The CCB is a complex automotive part with many features, which was chosen for measurement in this work for obtaining an accurate 3D point cloud. The data collection time was about two hours for each part. Our system scanned each part completely with six different poses. Data stitching was conducted with our proposed method and fiducial marker-based method. Quantitative comparisons were made by registering the measured data with CMM benchmarking data. In Fig. 8(a)(b), the point cloud

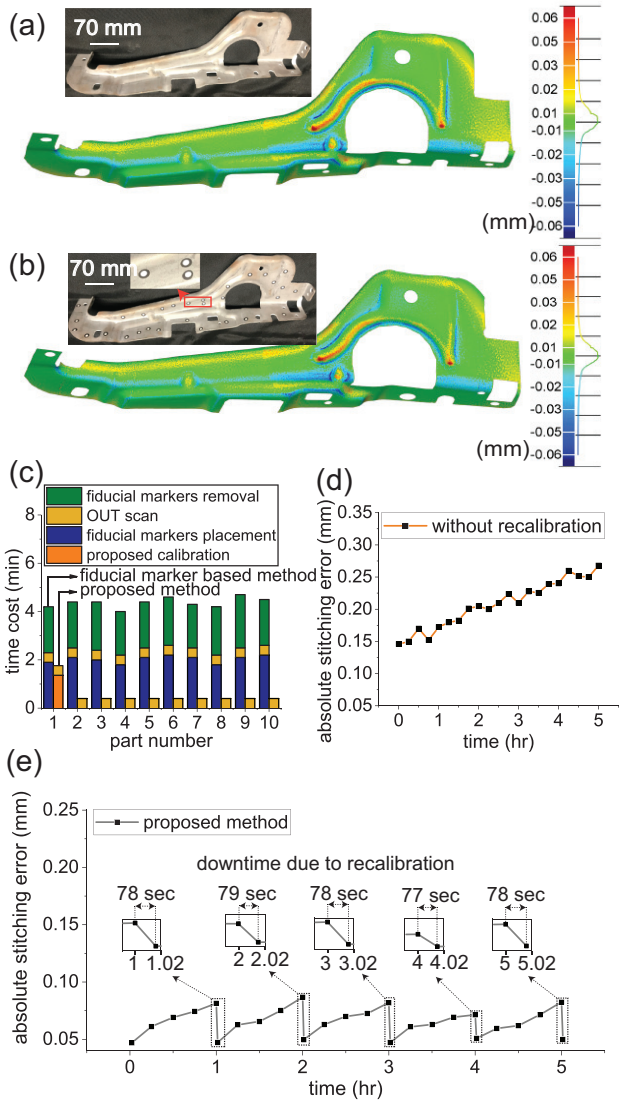

Fig. 8. Comparison of 3D point cloud obtained by our proposed method (a) and by fiducial marker-based method (b) with benchmarking data by CMM. (c) Comparison of time cost for measuring ten parts using the fiducial marker-based method and our proposed method. (d) Continuous operation of system for 5 hours without recalibration. (e) During 5-hr operation, recalibration was conducted after each hour.

areas with large positive and negative deviations from the point cloud obtained from benchmarking CMM are highlighted towards red and blue, respectively, while the green color denotes the least deviation. Compared to benchmarking data, our proposed method achieved a similar absolute data stitching error compared with the fiducial marker-based method.

Ten other different industrial parts such as front-end stamping parts, car beam bracket, and fuel filler door were then measured. To compare the time cost by our proposed method and the fiducial marker-based method, measurement was performed on these parts, as summarized in Fig. 8 (c). Manual steps such as marker placement and removal in the fiducial marker-based method caused an average downtime of 3.97 minutes for each part. Using our proposed method, calibration was performed once in the beginning, which caused 82 seconds (15 seconds for scanner calibration and 67 seconds

0278-0046 (c) 2020 IEEE. Personal use is permitted, but republication/redistribution requires IEEE permission. See http://www.ieee.org/publications_standards/publications/rights/index.html for more information.
Authorized licensed use limited to: The University of Toronto. Downloaded on August 22,2020 at 19:39:02 UTC from IEEE Xplore. Restrictions apply.

This article has been accepted for publication in a future issue of this journal, but has not been fully edited. Content may change prior to final publication. Citation information: DOI 10.1109/TIE.2020.3009568, IEEE Transactions on Industrial Electronics

for robot-scanner kinematic modelling and optimization). In subsequent recalibration when needed (e.g., after an hour of continuous scan/measurement), the downtime became lower than 82 seconds because the optimized values from the previous calibration were used as initial estimates in the next optimization run. For measuring the ten parts, the total time taken by the fiducial marker-based method was 43 minutes while our proposed method only took 7 minutes.

The system was then operated continuously for five hours without recalibration throughout the process (i.e., only using the traditional scanner calibration, initial DH parameters and hand-eye transformation) as summarized in Fig. 8 (d). For comparison, our proposed calibration method (including scanner calibration refinement and regular recalibration) was conducted after continuous measurement for each hour (downtime $\approx$ 78 seconds) as shown in Fig. 8 (e). The experimental results showed that the initial absolute stitching error of the proposed calibration method (about 0.05mm) was less than the error of traditional method without recalibration (about 0.15mm). In the traditional method without recalibration, absolute stitching error increased gradually over time due to increase in errors of DH parameters (up to 0.25mm). In contrast, the absolute stitching error is effectively maintained to be $<$0.1 mm with our proposed method, and each recalibration costs an average downtime of 78 seconds. Since the measurement without recalibration (Fig. 8 (d)) and with our proposed method (Fig. 8 (e)) were performed in separate operating conditions, and due to the random nature of environmental factors such as wear, temperature changes, and vibrations, differences in slopes of the error curves were observed.

Note that although state-of-the-art DH calibration techniques [20]–[23] could be integrated into traditional method to refine DH parameters for maintaining accuracy, the long downtime (e.g., about 10 minutes for mounting and removing specialized target [21], [22]) poses limitations for their application in long-term routine industrial use. These results prove that our proposed method is capable of achieving accurate 3D stitching and measurement, and the new calibration technique reduced the time cost of about 10 minutes by the traditional calibration method (DH calibration and hand-eye calibration separately) to averagely 78 seconds because the proposed method does not involve any manual steps such as attaching and removing specialized targets to the end-effector or require external optical/laser trackers for calibration. Note that the proposed method is applicable for hardware combinations with other robots (e.g., ABB and KUKA) and scanners (e.g., ZED [34] and Kinect [35]). The resultant absolute stitching error obtained after calibration using the proposed method would vary depending on the quality of hardware used.

VII. Conclusion

Since the accuracy of the scanner and the positioning accuracy of a robot manipulator deteriorates over time due to factors such as temperature changes, the errors in scanner's intrinsic parameters and robot's DH parameters cause inaccuracies in hand-eye transformation, leading to high 3D data stitching errors. This paper presented a new calibration method utilizing a novel scanner calibration technique, virtual arm-based kinematic model, trajectory-based robot-world transformation calculation, and nonlinear optimization. Using these techniques, the system achieved a low 3D data stitching error and a short calibration time. Experimental results showed that a low initial stitching error (0.0446 mm) was achieved after applying recalibration, the mean stitching error was effectively maintained to be $<$0.1 mm during the continuous measurement with an average intermittent downtime of 78 seconds for recalibration.

References

[1] S. von Enzberg and A. Al-Hamadi, "A multiresolution approach to model-based 3-d surface quality inspection," *IEEE Transactions on Industrial Informatics*, vol. 12, no. 4, pp. 1498–1507, 2016.

[2] A. Anwar *et al.*, "Quality inspection of remote radio units using depth-free image-based visual servo with acceleration command," *IEEE Transactions on Industrial Electronics*, vol. 66, no. 10, pp. 8214–8223, 2019.

[3] W. Lin *et al.*, "Recognition and pose estimation of auto parts for an autonomous spray painting robot," *IEEE Transactions on Industrial Informatics*, vol. 15, no. 3, pp. 1709–1719, 2019.

[4] Z. Xiong *et al.*, "Computational depth sensing : Toward high-performance commodity depth cameras," *IEEE Signal Processing Magazine*, vol. 34, no. 3, pp. 55–68, 2017.

[5] S. Barone *et al.*, "Three-dimensional point cloud alignment detecting fiducial markers by structured light stereo imaging," *Machine Vision and Applications*, vol. 23, no. 2, pp. 217–229, 2012.

[6] W. Liu *et al.*, "Global data registration technology based on dynamic coded points," *IEEE Transactions on Instrumentation and Measurement*, vol. 67, no. 2, pp. 394–405, 2017.

[7] G. A. Idrobo-Pizo *et al.*, "A calibration method for a laser triangulation scanner mounted on a robot arm for surface mapping," *Sensors*, vol. 19, no. 8, p. 1783, 2019.

[8] Q. Huang *et al.*, "Robotic arm based automatic ultrasound scanning for three-dimensional imaging," *IEEE Transactions on Industrial Informatics*, vol. 15, no. 2, pp. 1173–1182, 2018.

[9] P. I. Corke, "A simple and systematic approach to assigning denavit–hartenberg parameters," *IEEE Transactions on Robotics*, vol. 23, no. 3, pp. 590–594, 2007.

[10] R. Kluz *et al.*, "Investigations of temperature-induced errors in positioning of an industrial robot arm," *Journal of Mechanical Science and Technology*, vol. 32, no. 11, pp. 5421–5432, 2018.

[11] L. Ma *et al.*, "Modeling and calibration of high-order joint-dependent kinematic errors for industrial robots," *Robotics and Computer-Integrated Manufacturing*, vol. 50, pp. 153–167, 2018.

[12] S. Yin *et al.*, "Development and calibration of an integrated 3d scanning system for high-accuracy large-scale metrology," *Measurement*, vol. 54, pp. 65–76, 2014.

[13] Z. Zhang, "A flexible new technique for camera calibration," *IEEE Transactions on Pattern Analysis and Machine Intelligence*, vol. 22, no. 11, pp. 1330–1334, 2000.

[14] Z. Liu *et al.*, "High-accuracy calibration of low-cost camera using image disturbance factor," *Optics Express*, vol. 24, no. 21, pp. 24 321–24 336, 2016.

[15] Y. Yin *et al.*, "Calibration of fringe projection profilometry with bundle adjustment strategy," *Optics Letters*, vol. 37, no. 4, pp. 542–544, 2012.

[16] B. Li *et al.*, "Novel calibration method for structured-light system with an out-of-focus projector," *Applied Optics*, vol. 53, no. 16, pp. 3415–3426, 2014.

[17] Z. Tang *et al.*, "A precision analysis of camera distortion models," *IEEE Transactions on Image Processing*, vol. 26, no. 6, pp. 2694–2704, 2017.

[18] J. Ha *et al.*, "A stochastic global optimization algorithm for the two-frame sensor calibration problem," *IEEE Transactions on Industrial Electronics*, vol. 63, no. 4, pp. 2434–2446, 2015.

[19] J. Heller *et al.*, "Globally optimal hand-eye calibration using branch-and-bound," *IEEE Transactions on Pattern Analysis and Machine Intelligence*, vol. 38, no. 5, pp. 1027–1033, 2015.

[20] X. Zhang *et al.*, "Stereo vision based autonomous robot calibration," *Robotics and Autonomous Systems*, vol. 93, pp. 43–51, 2017.

[21] Gharaaty *et al.*, "Online pose correction of an industrial robot using an optical coordinate measure machine system," *International Journal of Advanced Robotic Systems*, vol. 15, no. 4, p. 1729881418787915, 2018.

0278-0046 (c) 2020 IEEE. Personal use is permitted, but republication/redistribution requires IEEE permission. See http://www.ieee.org/publications_standards/publications/rights/index.html for more information.
Authorized licensed use limited to: The University of Toronto. Downloaded on August 22,2020 at 19:39:02 UTC from IEEE Xplore. Restrictions apply.

This article has been accepted for publication in a future issue of this journal, but has not been fully edited. Content may change prior to final publication. Citation information: DOI 10.1109/TIE.2020.3009568, IEEE Transactions on Industrial Electronics

[22] A. Filion *et al.*, "Robot calibration using a portable photogrammetry system," *Robotics and Computer-Integrated Manufacturing*, vol. 49, pp. 77–87, 2018.

[23] Z. Jiang *et al.*, "A new kind of accurate calibration method for robotic kinematic parameters based on the extended kalman and particle filter algorithm," *IEEE Transactions on Industrial Electronics*, vol. 65, no. 4, pp. 3337–3345, 2017.

[24] A. Tabb and K. M. A. Yousef, "Parameterizations for reducing camera reprojection error for robot-world hand-eye calibration," in *2015 IEEE/RSJ International Conference on Intelligent Robots and Systems (IROS)*, pp. 3030–3037. IEEE, 2015.

[25] F. Dornaika and R. Horaud, "Simultaneous robot-world and hand-eye calibration," *IEEE Transactions on Robotics and Automation*, vol. 14, no. 4, pp. 617–622, 1998.

[26] J. Heller *et al.*, "Hand-eye and robot-world calibration by global polynomial optimization," in *2014 IEEE international conference on robotics and automation (ICRA)*, pp. 3157–3164. IEEE, 2014.

[27] C. Lu *et al.*, "Arc-support line segments revisited: An efficient high-quality ellipse detection," *IEEE Transactions on Image Processing*, vol. 29, pp. 768–781, 2019.

[28] R. Hartley and A. Zisserman, *Multiple view geometry in computer vision*. Cambridge university press, 2003.

[29] V. Lepetit *et al.*, "Epnp: An accurate o (n) solution to the pnp problem," *International Journal of Computer Vision*, vol. 81, no. 2, p. 155, 2009.

[30] A. Tröltzsch, "A sequential quadratic programming algorithm for equality-constrained optimization without derivatives," *Optimization Letters*, vol. 10, no. 2, pp. 383–399, 2016.

[31] S. H. E. A. Aleem *et al.*, "Optimal *c*-type passive filter based on minimization of the voltage harmonic distortion for nonlinear loads," *IEEE Transactions on Industrial Electronics*, vol. 59, no. 1, pp. 281–289, 2011.

[32] M. Adamczyk *et al.*, "Effect of temperature on calibration quality of structured-light three-dimensional scanners," *Applied Optics*, vol. 53, no. 23, pp. 5154–5162, 2014.

[33] M. Shah, "Solving the robot-world/hand-eye calibration problem using the kronecker product," *Journal of Mechanisms and Robotics*, vol. 5, no. 3, 2013.

[34] L. E. Ortiz *et al.*, "Depth data error modeling of the zed 3d vision sensor from stereolabs," *ELCVIA: electronic letters on computer vision and image analysis*, vol. 17, no. 1, pp. 0001–15, 2018.

[35] Z. Zhang, "Microsoft kinect sensor and its effect," *IEEE Multimedia*, vol. 19, no. 2, pp. 4–10, 2012.

Xingjian Liu (M'20) received the B.E. degree in Electronic Information Engineering from Huazhong University of Science and Technology, Wuhan, China, in 2013, and the Ph.D. degree in Materials Processing Engineering from the same university in 2018. He is currently working as a postdoctoral fellow at the Department of Mechanical and Industrial Engineering and the Robotics Institute, University of Toronto, Toronto, ON, Canada.

His research interests include computer vision, 3D sensing and metrology, and robotics.

Harikrishnan Madhsudanan (SM'20) received the B.Tech., degree in Mechatronics Engineering from SRM University, Chennai, India, in 2016. He worked as an Engineer with Fiat Chrysler Automobiles R&D, Chennai, India from 2016-2018. He is currently working toward the M.A.Sc degree in Mechanical and Industrial Engineering with the University of Toronto, Toronto, ON, Canada.

His research interests include robotics, kinematics, computer vision and automation..

Wenyuan Chen (SM'20) received the B.E. degrees in computer science from the Huazhong University of science and technology, Wuhan, China, in 2018. He is currently working toward the M.A.Sc degree in Electrical and Computer Engineering with the University of Toronto, Toronto, ON, Cannada.

His research interests include computer vision, deep learning and robotics.

Dahai Li received the B.S., M.S., and Ph.D. degrees in Mechanical Engineering from Xi'an Jiaotong University, Xi'an, China, in 2000, 2004, and 2010, respectively. He is currently working as a senior engineer in Xi'an Aerospace Propulsion Test Technology Institute, China. He visited University of Toronto as a visiting scholar from Oct, 2018 to Oct, 2019. His research interests include advanced metrology and machine learning.

Ji Ge (M'14) received the B.S. and M.S. degrees in mechatronics engineering from the Jiangxi University of Science and Technology, Ganzhou, China, in 2002 and 2005, respectively, and the Ph.D. degree in pattern recognition and intelligent system from Hunan University, Changsha, China, in 2012. He is currently a Post-Doctoral Fellow with the Department of Mechanical and Industrial Engineering, University of Toronto, Toronto, ON, Canada, and founder of Soochow InnoVision Technology Co., Ltd. His current research interests include machine learning and computer vision.

Changhai Ru received the Ph.D. degree in mechatronics engineering from the Harbin Institute of Technology, Harbin, China, in 2005. He was a Postdoctoral Fellow with the Department of Mechanical and Industrial Engineering, University of Toronto, Toronto, ON, Canada. He is currently a Professor with the Research Center of Robotics and Micro Systems and Collaborative Innovation Center of Suzhou Nano Science and Technology, Soochow University, China. His research interests include micro/nanomanipulation, nanopositioning technologies, and solid-state actuators? driving and control method.

Yu Sun (F'15) received the B.S. degree in electrical engineering from the Dalian University of Technology, Dalian, China, in 1996, the M.S. degree from the Institute of Automation, Chinese Academy of Sciences, Beijing, China, in 1999, and the M.S. degree in electrical engineering and the Ph.D. degree in mechanical engineering from the University of Minnesota, Minneapolis, MN, USA, in 2001 and 2003, respectively. He is currently a Professor at the University of Toronto. He is a Tier I Canada Research Chair and Director of the Robotics Institute. His lab specializes in developing innovative technologies and instruments for manipulating and characterizing cells, molecules, and nanomaterials. He was elected Fellow of ASME (American Society of Mechanical Engineers), IEEE (Institute of Electrical and Electronics Engineers), AAAS (American Association for the Advancement of Science), NAI (National Academy of Inventors), CAE (Canadian Academy of Engineering), and RSC (Royal Society of Canada) for his work on micro-nano devices and robotic systems.

0278-0046 (c) 2020 IEEE. Personal use is permitted, but republication/redistribution requires IEEE permission. See http://www.ieee.org/publications_standards/publications/rights/index.html for more information.
Authorized licensed use limited to: The University of Toronto. Downloaded on August 22,2020 at 19:39:02 UTC from IEEE Xplore. Restrictions apply.